AIAA JOURNAL
Vol. 45, No. 9, September 2007

Diode-Laser Sensor for Air-Mass Flux 1: Design and Wind-Tunnel Validation

Kent H. Lyle,* Jay B. Jeffries,† and Ronald K. Hanson‡
Stanford University, Stanford, California 94305

DOI: 10.2514/1.26360

The design and construction of a fiber-coupled diode-laser sensor to determine air-mass flux via separate measurements of the velocity and density of oxygen in air is reported. The density is determined from the spectroscopic absorption of an oxygen feature in the A-band near 764 nm, while the velocity is obtained from the Doppler frequency shift between the absorption features from two crossed paths within the flowfield (wind-tunnel path length 1.07 m). A hybrid operation is used for this sensor, in which rapidly alternating (50 Hz) measurements are made: direct absorption for the density and wavelength modulation for velocity. The sensor's performance is validated using a well-characterized low-speed wind tunnel which provided uniform flows up to 23 m/s. The results showed that the sensor is able to measure a time-averaged velocity to within 0.25 m/s and a time-averaged density to within 0.7% of the tunnel set point, with corresponding 1-s standard deviations of 0.22 m/s and 0.76%, respectively. The mean mass flux accuracy was assessed and a 1-s standard deviation of 1.3% was measured at the highest flow rates.

Nomenclature

A	=	integrated absorbance, cm^{-1}
a	=	amplitude of laser WMS modulation, cm^{-1}
c	=	speed of light in a vacuum, m/s
f	=	laser modulation frequency, Hz
H_k	=	absorption Fourier harmonic function
$I(\nu)$	=	laser intensity, including absorption
$I_0(\nu)$	=	baseline laser intensity without absorption
i_0	=	modulation intensity amplitude
k_ν	=	spectral absorption coefficient
L	=	laser path length through absorbing medium, cm
$\dot{m}_{\text{meas}}$	=	time-averaged measured mass flow, kg/s
P	=	gas pressure, atm
P_i	=	partial gas pressure of species i, atm
R	=	mass-based gas constant, $m^3 \cdot atm/(kg \cdot K)$
$S(T)$	=	temperature-dependent line strength, $cm^{-1}/(cm \cdot atm)$
$S_2(\bar{\nu})$	=	signal output function for WMS-2f
t	=	time, s
U	=	bulk gas velocity, m/s
X_i	=	mole fraction of species i
α	=	lock-in amplifier phase angle, deg
$\Delta\nu$	=	Doppler-shifted difference between line-center frequencies, cm^{-1}
$\varepsilon_{\%,\text{ave}}$	=	percent accuracy of time-averaged mass flux measurement
$\varepsilon_{\%,1\text{ s}}$	=	estimated percent accuracy for 1-s mass flux measurements
θ	=	crossing half-angle between two beams in measurement test section
ν	=	optical frequency, cm^{-1}
ν_0	=	line-center frequency in absence of Doppler shift, cm^{-1}
ρ	=	gas density, kg/m^3
$\sigma_\%$	=	percent 1-s standard deviation of mass flux measurement
τ_ν	=	transmittance through an absorbing medium
$\phi(\nu)$	=	normalized line shape function, cm
$\chi(\nu)$	=	fraction of light absorbed
ψ	=	intensity modulation phase shift, rad

Received 7 July 2006; revision received 22 January 2007; accepted for publication 27 February 2007.

*Graduate Research Assistant, Mechanical Engineering; Present Address: GE Aircraft Engines, Cincinnati, OH. Member AIAA.

†Senior Research Engineer, Mechanical Engineering. Associate Fellow AIAA.

‡Professor, Mechanical Engineering. Fellow AIAA.

I. Introduction

THE measurement of gas mass flux, that is, the product of velocity and density, is valuable for many applications. For aeroengines, the inlet air-mass flux is used in evaluations of combustor performance, engine thrust, and ram drag, that is, the drag induced by the momentum flux of air into the inlet [1]. Mass flux is also useful for characterizing inlet flow distortion resulting from the angle of attack of the aircraft [2]. The current standard for measuring mass flux at ground-test facilities is through the use of total and static pressure probes and total temperature or thermocouple probes [2–4]. This instrumentation requires the installation of an instrumented bell mouth upstream of the inlet, and in some cases also a spoke-and-ring "wagon wheel" in front of the bell mouth. The requirement of special external hardware limits the method to ground tests. In the absence of any external instrumentation, in-flight air flow rates are conventionally calculated using a combination of the fan speed, the pressure ratio across the fan, and the inlet air temperature, all of which have been calibrated to a specific mass flow based on extensive ground testing of the particular engine [1]. To the extent that the engine operates at steady state near its design point, the inferred mass flux is very accurate. However, transient conditions and deviations from optimal operating conditions can reduce accuracy significantly. Thus, there is a need for a nonintrusive, real-time (i.e., on-line data analysis without postprocessing) mass flux sensor that could be used for in-flight qualification testing and potentially even a closed-loop control system.

Tunable diode-laser absorption spectroscopy has been proven for rapid gas measurements in practical environments for over a decade. Variations of this technique have been used to infer temperature, species mole fraction, pressure, velocity, and even density [5–8]. In typical practice, the laser is rapidly tuned across absorption features, and the transmitted laser radiation is recorded by a photodetector to yield spectrally resolved absorption lines (see Fig. 2). Room temperature diode lasers have been used to measure water vapor [9], CO and CO_2 [10], O_2 [11], and NH_3 [12], among other species. These sensors have been used in aeroengine inlets [8], incinerators [13], scramjets [14], pulse detonation engines [15], piston engines [16],

hypersonic wind tunnels [17], and other realistic and harsh environments. Cryogenically cooled, mid-infrared diode lasers have also been used to measure velocity of NO in hypersonic wind tunnels [18,19].

The sensor described here builds upon a body of work initiated by Philippe and Hanson [7], who measured the velocity, temperature, and pressure of O_2 in a shock tube using a distributed feedback (DFB) laser to probe individual features in the O_2 A-band near 762 nm. Wavelength modulation with second-harmonic ($2f$) detection was used to increase measurement sensitivity, speed, and accuracy. Further extension of this concept was reported in a patent [20] which proposed methods of using either absorption or fluorescence to measure gas velocity and density to determine the thrust of a jet combustor. The work of Miller et al. [8] continued the development of this concept for ground-test measurements of subsonic air-mass flux in a Pratt and Whitney F-100 turbofan engine using diode-laser absorption of O_2. Instead of wavelength modulation, direct absorption with balanced ratiometric detection was used to obtain high-accuracy velocity and density measurements. In contrast to Philippe and Hanson [7] who measured temperature and pressure separately, density was obtained from a single absorption measurement. The best-case accuracy of the sensor was assessed at 1–2% with postprocessing, with a predicted accuracy of 3–4% when configured at conditions that would allow for operation with 1 Hz readout.

The current work combines the advantages of wavelength-modulation spectroscopy with $2f$ detection (WMS-$2f$) for high-accuracy Doppler velocity measurements with the single-feature density measurement described by Miller et al. [8]. The sensor makes use of fiber-optic coupling and a single absorption line in the A-band of molecular oxygen near 764 nm. First, the fundamental principles of the sensor are discussed, the hardware implementation is described, and finally test measurements of simultaneous velocity and density are reported with a readout rate of 1 Hz in a calibrated low-speed wind tunnel at Stanford University. In a companion paper [21], this sensor is used for inlet mass flux measurements during ground test of a commercial Pratt and Whitney aircraft engine.

II. Measurement Methodology for Density

The oxygen A-band consists of rovibronic transitions centered near 762 nm between the upper state $b^1\Sigma_g^+(v'=0)$ and the lower state $X^3\Sigma_g^-(v''=0)$. This band has been widely used in the study of molecular oxygen [7,8,11,22–24]. An absorption transition from this band is measured by scanning the diode laser across the feature and quantifying the attenuation of the laser intensity using a photodetector. The transmittance of the laser intensity $\tau(\nu)$ at frequency ν along a uniform path is given by the Beer–Lambert relation:

$$\tau(\nu) = \frac{I(\nu)}{I_0(\nu)} = \exp(-k_\nu L) \tag{1}$$

where $I(\nu)$ is the transmitted radiation intensity, $I_0(\nu)$ is the intensity in the absence of absorption, and k_ν is the spectral absorption coefficient expressed in units of cm^{-1}, equivalent to an absorption per unit length. The product of k_ν and L is referred to as the absorbance. Figure 1a shows the experimentally measured transmittance from the PP(11,11) (spectroscopic notation following [22]) absorption feature at 764.28 nm, and Fig. 1b displays the resulting absorbance of that feature using Eq. (1). In practice, the diode-laser wavelength is scanned via variation of the injection current as a function of time, which is calibrated with a solid Fabry–Perot etalon with a free spectral range of 2 GHz (0.067 cm^{-1}). The etalon has a tolerance of ± 0.0025 GHz (8.3×10^{-5} cm^{-1}) which represents the precision of the x axis in Fig. 1. The accuracy of the wavelength scale is limited by the well-known line center of the oxygen absorption feature. If it is assumed that there is only one absorbing species and one spectroscopic transition, the absorption coefficient can be expressed as

$$k_\nu = PX_iS(T)\phi(\nu) \tag{2}$$

Here P (atm) is the static pressure of the mixture, X_i is the mole fraction of absorbing species i, $S(T)$ ($cm^{-1}/cm \cdot atm$) is the temperature-dependent line strength of the transition, and $\phi(\nu)$ (cm) is the normalized line shape function.

The integrated area of the absorbance curve shown in Fig. 1b, obtained by integrating absorbance over all values of frequency, is given by $A = PX_iS(T)L$. Miller et al. [8] pointed out that the integrated absorbance of the PP(11,11) feature at 764.28 nm is directly proportional to the partial density of oxygen to within a tolerance band of $\pm 1\%$ from 235 to 320 K. Thus, the integrated absorbance can be directly related to the oxygen density, which is itself directly proportional to the air density assuming that the value of X_{O2} is known. For dry air, X_{O2} is 0.2095, but at 296 K and 1 atm this value reduces to 0.2029 at 100% relative humidity, a difference of 1.2%. The water vapor contributes not only to the O_2 mole fraction but also to the value of the mixture molecular gas constant, increasing it by as much as 1% from its dry air value of 287 $J/(mol \cdot K)$. Thus, precise measurements require a correction for relative humidity. The presence of water vapor can also have an effect on the pressure broadening coefficients of the oxygen transition, but the mass flux

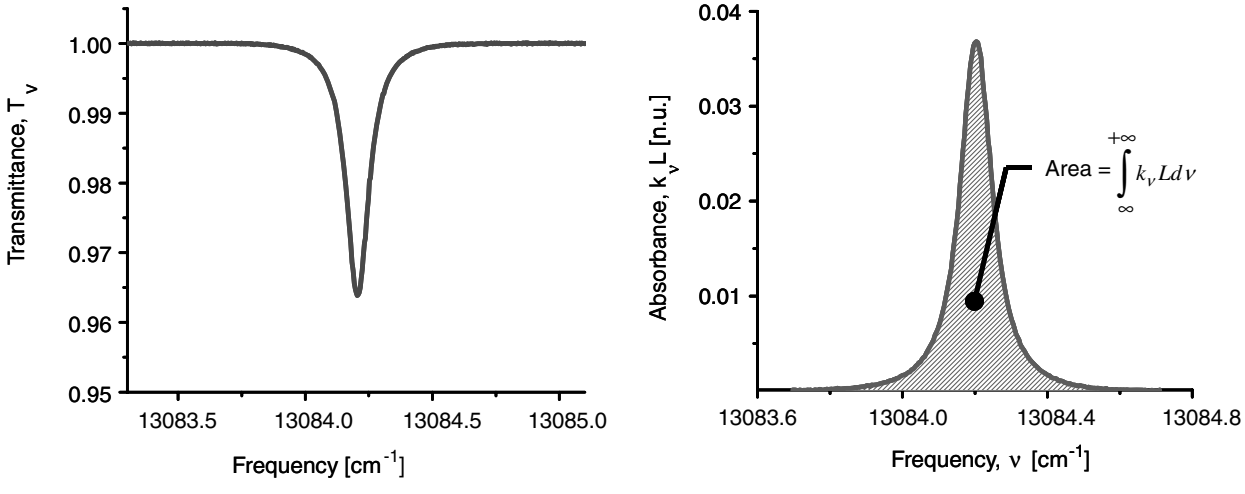

Fig. 1 a) Experimental transmittance as laser beam is scanned across the PP(11,11) absorption feature at 764.28 nm, averaged over 20 scans ($T = 294$ K, $P = 1$ atm, $X_{O2} = 20.6\%$, $L = 164$ cm). b) Absorbance of the feature shown in a).

measurement schemes described here are not sensitive to the transition width, and the variation of pressure broadening does not have an influence on measurement accuracy.

III. Measurement Methodology for Velocity

If the gas has a component of uniform bulk velocity which is parallel to the beam path, the absorption feature will experience an apparent shift in its line-center frequency. The magnitude of this shift is given by

$$\frac{\Delta\nu}{\nu_0} = \frac{\boldsymbol{U}\cdot\boldsymbol{k}}{c} \tag{3}$$

where $\Delta\nu$ ([cm^{-1}) is the shift of the line-center frequency, ν_0 (cm^{-1}) is the unshifted line center, c is the speed of light (3×10^8 m/s), $\boldsymbol{U}$ (m/s) is the velocity vector of the gas stream, and $\boldsymbol{k}$ is the unit direction vector of the laser beam. Note that $\Delta\nu$ will be positive when the dot product of $\boldsymbol{U}$ and $\boldsymbol{k}$ is positive. Figure 2 shows a schematic of the mass flux sensor installed in a duct with a uniform velocity U in which the laser output is split into two identical beams, one of which points upstream at an angle θ to the perpendicular while the other points downstream at the same angle. The frequency difference between the two line centers then becomes

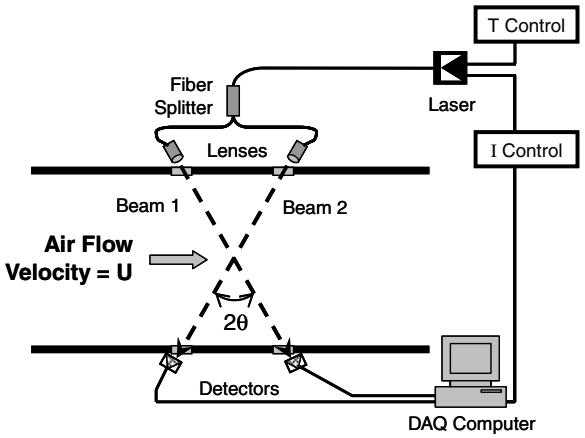

Fig. 2 Schematic of the mass flux sensor.

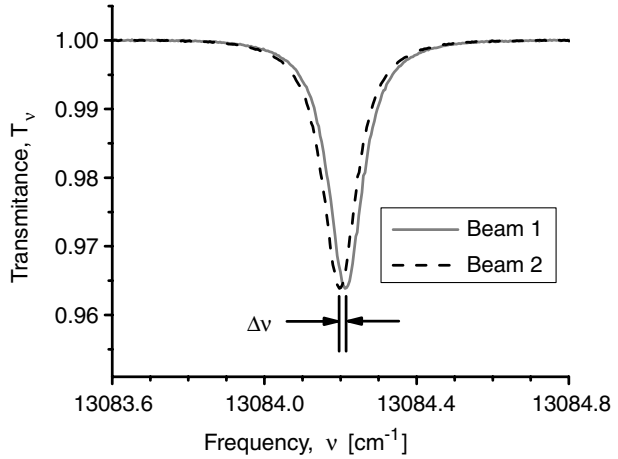

Fig. 3 Transmittance as laser beams are scanned across the absorption feature at 764.28 nm with a simulated Doppler shift of $\Delta\nu = 0.0154$ cm^{-1} corresponding to $U = 250$ m/s and $2\theta = 90$ deg ($T = 294$ K, $P = 1$ atm, $X_{O2} = 20.6\%$, $L = 164$ cm).

$$\Delta\nu = \frac{(2\sin\theta)U}{c}\nu_0 \tag{4}$$

Figure 3 shows the transmittance of both beams scanned across the O_2 absorption feature located at 764.28 nm with a simulated frequency shift of $\Delta\nu = 0.0154$ cm^{-1} (460 MHz) which corresponds to a flow velocity of 250 m/s and $2\theta = 90$ deg. At 296 K and 1 atm, the full-width at half-maximum (FWHM) of the feature is about 0.1 cm^{-1} (3 GHz), which means that the observed shift is 15% of the FWHM. At 100 m/s, this shift reduces to 6.2×10^{-3} cm^{-1} (185 MHz), or 6.1% of the FWHM. This is why diode-laser velocimetry has traditionally been used for high-speed applications such as hypersonic wind tunnels, where velocities of NO [18,19] and H_2O [17] within the range of 2500 to 4500 m/s were measured. If a target accuracy of 1% is to be achieved at 100 m/s, then the sensor must be able to resolve velocities on the order of 1 m/s, which means measuring frequency shifts of 6.2×10^{-5} cm^{-1} (1.85 MHz), or 1/1600 of the feature's FWHM. Note that this shift is on the order of a typical diode-laser linewidth, 1–5 MHz. However, this linewidth only broadens the observed absorption feature by a relatively small amount compared to other broadening mechanisms. The measured velocity depends on the difference between the absorption line center of two measurements, and the challenge to achieve high measurement precision is the ability to distinguish a small Doppler frequency shift from much larger widths of the absorption features. To experimentally achieve this high precision, it is essential to employ a technique which ensures a high signal-to-noise ratio and minimizes other sources of measurement uncertainty such as baseline fitting. This goal is accomplished through the use of scanned-wavelength-modulation spectroscopy with $2f$ detection.

WMS is a well-established technique for obtaining higher signal-to-noise ratios than would be achieved using direct absorption. It has been described in detail by previous researchers [7,25–29] and will only be briefly summarized here. In its scanned-wavelength configuration, WMS consists of superimposing a high-frequency sine wave onto a slow linear ramp. The equations for the laser instantaneous output frequency and intensity can be expressed as

$$\nu(t) = \bar{\nu}(t) + a\cos(2\pi ft) \tag{5}$$

$$I_0(t) = \bar{I}_0(t) + i_0\cos(2\pi ft + \psi) \tag{6}$$

In the above equations, $\bar{\nu}(t)$ (cm^{-1}) and $\bar{I}_0(t)$ (mW) represent the components of the optical frequency and laser intensity resulting from the slow ramp, while a (cm^{-1}) and i_0 (mW) are the corresponding amplitudes of modulation for the sinusoidal components. The a parameter is sometimes referred to as the modulation depth. The modulation frequency is f (Hz), while the phase shift is ψ. For an ideal laser, $\psi = \pi$, because diode lasers will scan downward in optical frequency as the forward current is increased. In practice, however, there is a time lag between the response of the laser output intensity and the optical frequency, so that ψ will be $>\pi$, with the exact value depending upon the laser characteristics and the frequency of modulation.

When combined with the fraction of light which is absorbed, $\chi(\nu) = 1 - \tau(\nu)$, Eq. (6) can be used to express the transmitted laser intensity, $I(t)$.

$$I(t) = [\bar{I}_0(t) + i_0\cos(2\pi ft + \psi)]\{1 - \chi[\nu(t)]\} \tag{7}$$

Because the absorption function $\chi(\nu)$ follows the frequency modulation with no phase delay, it can be expanded as a periodic, even function of $2\pi ft$ in a Fourier cosine series:

$$\chi[\bar{\nu}(t) + a\cos(2\pi ft)] = \sum_{k=0}^{\infty} H_k(\bar{\nu}, a)\cos(k2\pi ft) \tag{8}$$

The harmonic functions H_k are described by

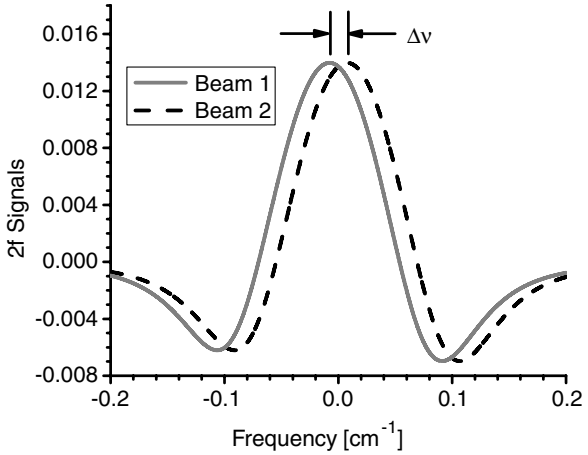

Fig. 4 $2f$ absorption signals obtained from lock-in amplification of experimental WM scans including simulated frequency shift of 0.0154 cm^{-1}, averaged from 20 scans at 50 Hz (mod$f$ = 20 kHz, a = 0.09 cm^{-1}).

$$H_k(\bar{\nu}, a) = \frac{1}{(1+\delta_{0k})\pi}\int_{-\pi}^{+\pi} \chi(\bar{\nu} + a\cos u)\cos(ku)\,\mathrm{d}u \qquad (9)$$

where the delta function δ_{0k} is equal to unity when $k = 0$, and is equal to zero otherwise.

The measured intensity is processed through a lock-in amplifier, which consists of a mixer and a low-pass filter. For second-harmonic detection, the mixer multiplies the signal by a cosine wave with frequency $2f$ and phase angle α. The low-pass filter removes all high-frequency content, with the remaining absorption signal being described by

$$S_2(\bar{\nu}) = -\frac{i_0}{4}H_1(\bar{\nu})\cos\psi - \frac{1}{2}\bar{I}_0(\bar{\nu})H_2(\bar{\nu}) - \frac{i_0}{4}H_3(\bar{\nu})\cos\psi \qquad (10)$$

where it has been assumed that $\alpha = 0$. The $\bar{I}_0$ term is expressed as a function of $\bar{\nu}$ simply because both terms are linear functions of t; this formalism permits the removal of all time-dependent terms from Eq. (10). Figure 4 shows an example of two $2f$ signals with a simulated Doppler frequency shift of 0.0154 cm^{-1}, which corresponds to a velocity of 250 m/s with a laser beam crossing angle of 90 deg.

There are several advantages of using WMS-$2f$. First, because the detection occurs at harmonics of the modulation frequency, much of the low-frequency noise is filtered out, including laser noise and mechanical vibrations. The mass flux sensor uses a modulation frequency of 20 kHz, which is sufficiently high for effective low-frequency filtering but still low enough for good digital resolution. Second, in the limit of linear laser intensity response with injection current, the signal resides on a zero background, which eliminates the need to obtain a baseline. A third advantage is that because the $2f$ detection ignores the dc-component of the signal, ac-coupling can be used to filter out the low-frequency background and increase the dynamic range of the signal. This effectively increases the resolution of the analog-to-digital (A/D) sampling system, which was 12 bits for this sensor.

Figure 5 shows $2f$ absorption signals obtained from a measurement made in the Stanford wind tunnel operating at 2 m/s using the configuration shown in Fig. 9. The Doppler shift is too small to be visually observed in the plot of the full WMS-$2f$ line shape (Fig. 5a). However, when the scale is expanded to zoom in on a small region of the WMS-$2f$ line shape (see Fig. 5b), the frequency difference of 1.3×10^{-4} cm^{-1} is observed, which corresponds to a velocity of 2.1 m/s for a crossing angle of 90 deg. This frequency difference measurement can be repeated at multiple locations on the WMS-$2f$ line shape; typically 100 evenly spaced locations are used for each measurement, and the average value provides the line center with a precision of roughly one part in 10^3 of the FWHM.

The superiority of WMS-$2f$ detection for Doppler shift measurements can be shown in Fig. 6, which shows Doppler frequency shift measurements in quiescent air, in units of MHz, made using direct absorption (left) and scanned WMS-$2f$ (right). Note that at a crossing angle of $2\theta = 45$ deg, a 1 MHz frequency shift corresponds to a velocity of 1 m/s. The direct absorption measurements were made by ramping the laser with a sawtooth driving function at 50 Hz and using a Voigt-fitting routine to determine the line centers of both features to determine the Doppler shift. The scanned WMS-$2f$ measurements were made by combining a 50 Hz ramp with a 20 kHz modulation function. For both sets of measurements, each data point was obtained from 20 consecutive laser scans which were averaged together before processing to reduce noise. It is readily apparent that the Voigt-based direct absorption results exhibit much greater scatter than the WMS-$2f$-based values. In fact, a ratio of the standard deviations from the two methods shows that the WMS-$2f$ measurements offer a noise reduction of 90% over the Voigt measurements. This makes WMS-$2f$ attractive for subsonic velocity measurements.

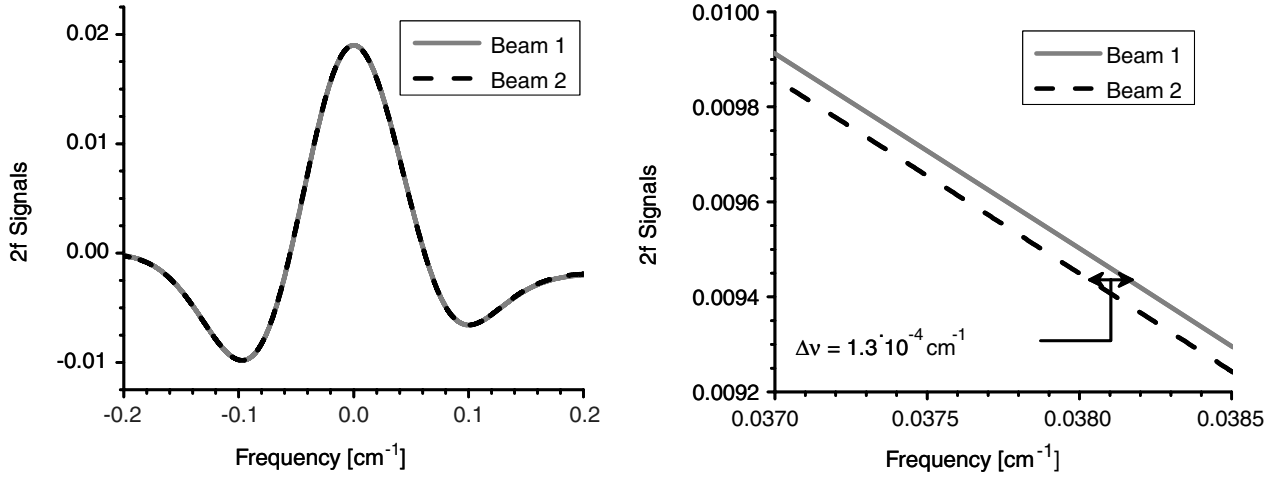

Fig. 5 Sample $2f$ absorption signals obtained from the Stanford wind tunnel operating at 2 m/s: a) full $2f$ signals; b) magnified to show Doppler shift. (mod$f$ = 20 kHz, a = 0.09 cm^{-1}).

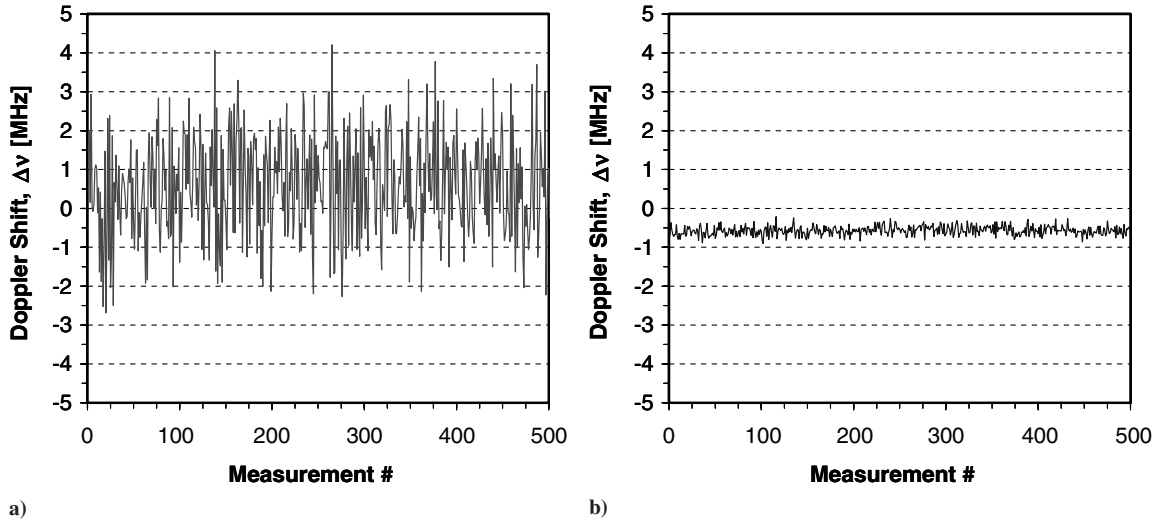

Fig. 6 Doppler shift measurements made in quiescent air at a 50 Hz scanning rate with 20 scan averaging using a) direct absorption and b) scanned WMS-2*f*.

IV. Sensor Description

The heart of the mass flux sensor is the diode laser itself, of which two types were employed. The earlier version of the sensor used a CSEM760 VCSEL (vertical cavity surface emitting laser) (C463VGD3) which was in the form of a TO-39 can package and produced a maximum intensity of about 0.5 mW. This VCSEL was not directly fiber coupled and required external optical coupling equipment, namely, an optical isolator and a fiber capture lens. The later version used a Nanoplus 764 nm DFB (153/4-20) in a fiber-pigtailed TO-5.6 package. The Stanford wind-tunnel testing used the readily available VCSEL laser whose sensitive wavelength tuning with injection current reduces potential errors in the baseline fitting for the direct absorption density measurement. However, the VCSEL required external optics to couple the light into the fiber, and the power output was much lower than that of the DFB, 0.2 mW versus 3 mW. Although the VCSEL was superior in the laboratory, the higher power DFB was more desirable in harsh environments of the aeroengine tests, described in a companion paper [21]. In general, the experiences with both the VCSEL and DBF lasers are in agreement with the conclusions of Weldon et al. [30], who describe a detailed comparison between a VCSEL and DFB near 762 nm.

Both lasers were mounted in a temperature-controlled ILX Lightwave LDM-4412 diode-laser mount. The VCSEL configuration also included an aspheric collimating lens (Optima Precision, Inc.) with a focal length of 4 mm mounted directly in front of the laser emitting surface. The lens was antireflection coated for 780 nm to avoid interference owing to internal reflections and produced a beam diameter of approximately 1 mm. An ILX Lightwave LDT-5910B temperature controller was used to maintain the operating temperature of the mount. The laser operating current was controlled by an ILX Lightwave LDC-3620 ultralow-noise current source. This controller had the advantage of running entirely on battery power, which eliminated ac line noise and allowed for lower noise operation. This was especially important for the VCSEL, whose wide tuning characteristics made it very vulnerable to noise sources at narrow scan widths. The hybrid WM/direct scanning function was generated by the DAQ computer using a 12-bit National Instruments PCI-6115 A/D board.

Figure 2 showed a schematic of the hardware components of the mass flux sensor. The laser was coupled via a single mode (SM) fiber to a 50/50 Oz Optics 1 × 2 fiber splitter. Both legs were connected to the remote transmitting optics through the use of relatively long fiber patch cables, which were 5 m long for the Stanford wind-tunnel tests. The transmitting optics themselves consisted of Thorlabs F230FC-B fiber collimating lenses, which had a focal length of 4.5 mm and produced a beam diameter of approximately 1 mm. Both lenses were mounted on Newport LP-05A multi-axis lens positioners, which allowed for the precise adjustment of translational location and angular tilt of the beams. The collimated beams emanating from the lenses each passed through a wedged window into the test section; the short distance between the lens and the window was not purged of ambient oxygen. Both beams traversed the test section at a crossing angle of 2θ, and passed through two more wedged windows on the opposite side of the test section. From there, both beams were focused using 25 mm focal length concave mirrors onto the Thorlabs PDA55 silicon photodetectors. These detectors had an active diameter of 3 mm, and an upper cutoff frequency of 0.7–10 MHz depending upon the gain setting. As was the case with the transmitting optics, the short optical path (<10% of the path inside of the wind tunnel) between the window and the detector was not purged.

V. Sensor Operation

The laser was scanned at a repetition rate of 50 Hz. During successive scans, the sensor alternated between modes of a linear wavelength scan for direct absorption and a linear scan with sinusoidal modulation for WMS. During the wavelength-modulation scan, a 20 kHz sine wave was superimposed on the linear ramp, with a modulation amplitude a of 0.09 cm^{-1} that was approximately 1.8 times the half-width at half-maximum (HWHM) of the absorption feature. The data acquisition computer collected a block of data from each channel at a digital sampling rate of 2 MS/s (megasamples/second) over a prescribed number of scans. Figure 7 provided a schematic representation of the processing of these

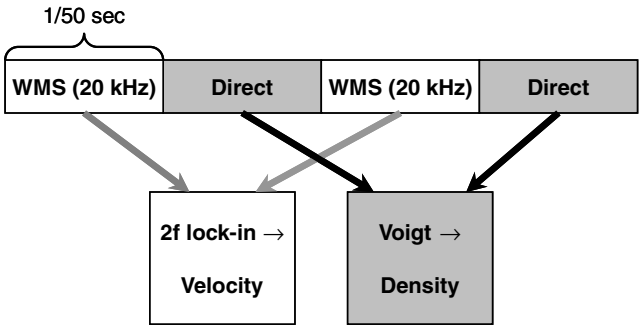

Fig. 7 Schematic of data reduction for hybrid direct/WMS sensor operation.

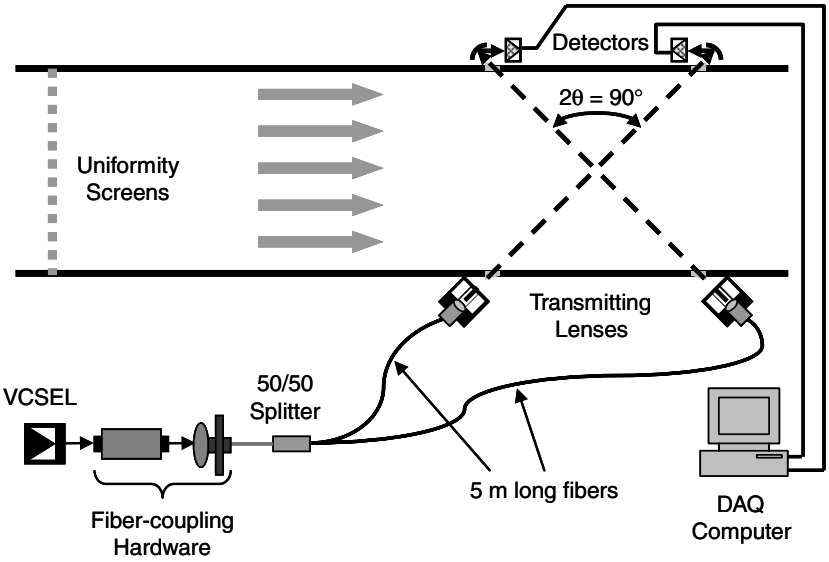

Fig. 8 Schematic of the mass flux sensor installed in the Stanford wind tunnel.

alternating direct absorption and WMS-2f signals by the Labview-based software. The wavelength-modulated scans from the ac-coupled outputs of both detectors were selected from both data blocks, bulk averaged across the individual scans to reduce noise content, and then processed through software-based lock-in amplifiers. This software lock-in consisted of a mixer, which multiplied the raw signal by a sine wave at twice the modulation frequency, and a low-pass filter, which removed all high-frequency content from the resulting WMS-2f signals. Meanwhile, the direct absorption data from the dc-coupled output from one of the detectors were selected from the data block, bulk averaged across individual scans to reduce noise content, and then processed using a Voigt-fitting routine. The data processing was sequential, in that the Labview program alternated between acquiring data blocks from the input board and performing calculations for the velocity and density measurements. In practice, this meant that the program collects 34 out of 50 laser scans during each readout cycle due to processor downtime. Nonetheless, there was sufficient time during each 1 Hz cycle for the sensor to report velocity and density simultaneously with sufficiently high precision.

VI. Low-Speed Wind-Tunnel Validation Facility

The test bed for the qualification of the mass flux sensor was a low-speed wind tunnel at Stanford; this open-circuit tunnel consisted of a front-mounted compressor, a converging transition section preceded by a series of uniformity screens, and a long constant area 76×76 cm^2 square section. The tunnel was capable of producing velocities up to $\sim$23 m/s and was calibrated to an accuracy within $\pm 1\%$ of the full scale flow rate. In addition, the freestream velocity profile was known to be uniform to within $\pm 1\%$. Although the tunnel velocities were relatively low compared to our target velocity range of $>$100 m/s, the facility provided a well-characterized test bed to assess the sensor's ability to measure subsonic velocities.

Figure 8 shows a schematic of the mounting of the sensor in the wind tunnel, in which the VCSEL beam was split into two paths by the 50/50 fiber splitter and transmitted to the lenses mounted on one side of the wind tunnel. Both beams were pitched through 7 deg wedged windows at a crossing angle of 90 deg. Each beam traversed a total path length of 108 cm within the measurement section before reaching the second set of 7 deg wedged windows, after which the light was focused onto Thorlabs PDA55 photodetectors (3 mm active diameter, 2.3 MHz) using 25 mm focal length focusing mirrors. The short stagnant regions outside of the wind tunnel, represented by a length of L_{stag}, which totaled to less than 18% of the tunnel measurement path, represented by the length L_{flow}, were not purged to remove ambient oxygen, and their contribution to the measured velocity was removed by using a ratio of the total laser path to the flow path within the tunnel:

$$U_{0,\text{corr}} = U_{0,\text{meas}} \frac{L_{\text{flow}} + L_{\text{stag}}}{L_{\text{flow}}} \tag{11}$$

The influence of the thin boundary layers ($<$3 mm) was determined to be below the sensor's precision level at these low flow rates, and velocity data corrections were not necessary for this effect.

VII. Results and Discussion of Wind-Tunnel Validation

The results of a typical wind-tunnel test are shown in Fig. 9 where gas density and velocity measured with the tunable diode-laser-based subsonic mass flux sensor are plotted versus time as the wind-tunnel flow is adjusted through 11 different set points. The black diamonds indicate the tunnel set point, while the gray and black curves represent the measured velocity and density, respectively. The tunnel

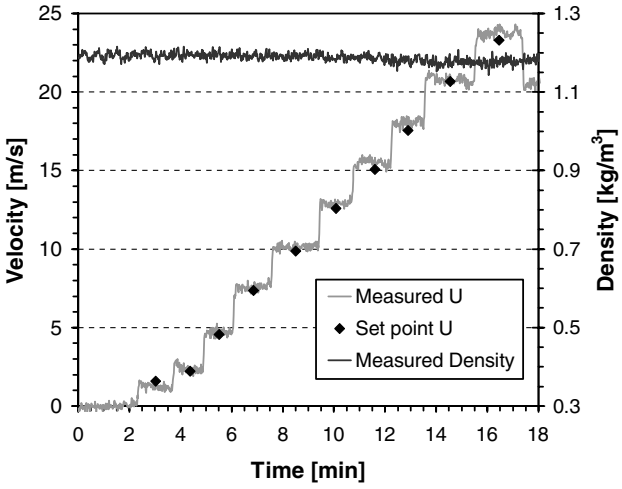

Fig. 9 Typical velocity and density measurements from the Stanford wind tunnel. (1 Hz, $2\theta = 90$ deg).

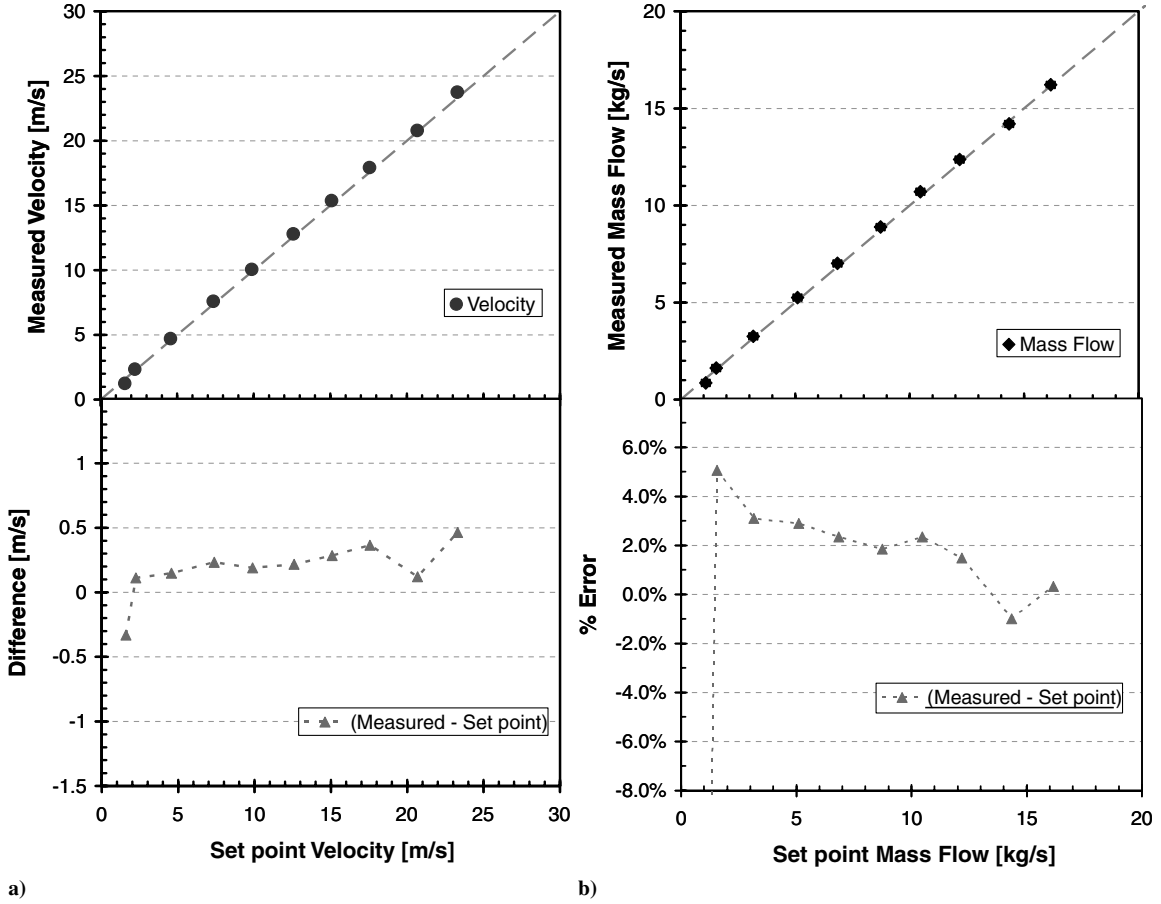

Fig. 10 Comparison of time-averaged sensor-based measurements to set point for velocity a) and mass flow b) for data from Fig. 9. Differences also shown. (1 Hz, $2\theta = 90$ deg).

was stepped up to successively higher velocities and allowed to operate at steady state for several minutes at each velocity. The mean measured velocity at each time-averaged condition is always within 0.5 m/s of the set point. The overall mean measured density is within 0.7% of the ambient room density, with a standard deviation of 0.76% relative to the mean measured value. The laser sensor data are provided at 1 Hz readout rate without postprocessing. The downward drift of gas density at times greater than 10 min is thought to be due to the slight heating of the air from the continuous operation of the compressor. An independent thermometer measurement indicated that the air temperature increased by over 2 K over the full test duration.

A detailed comparison of the time-averaged laser sensor measurements with the wind-tunnel calibrated set point values are shown in Fig. 10 for velocity (left panels) and mass flow (right panels). The mean difference between the measured and the set point velocity is 0.25 m/s, and the overall standard deviation of instantaneous velocity is 0.22 m/s. The time-averaged mass flow is obtained using the following equation:

$$\bar{\dot{m}}_{\text{meas}} = \frac{\sum_{n=i}^{i+N-1} U_{\text{meas}}(t_n)\rho_{\text{meas}}(t_n)A_{\text{tunnel}}}{N} \tag{12}$$

where N is the total number of instantaneous (1-second) data points used for the mean measurement and A_{tunnel} is the cross-section area of the tunnel (0.581 m^2). The percentage difference between the laser sensor measured mass flows and the tunnel calibrated flow is plotted in the lower right panel of Fig. 10. The standard deviation of the instantaneous mass flow at 23.3 m/s is 0.2 kg/s. At the two highest flow rates, the difference between the mean measured mass flow and the set point mass flow is $\leq 1\%$, which is within the combined tunnel set point velocity and density uncertainty of 1.1%.

An estimate of the expected sensor accuracy at higher velocities is determined from an extrapolation of the results in Fig. 10. We assume the accuracy of the mass flow sensor can be deduced from the time-averaged data as

$$\varepsilon_{\%,\text{ave}} = \frac{\bar{\Delta}_{\dot{m}}}{\dot{m}_{\text{sp}}} \times 100\% \tag{13}$$

where $\varepsilon_{\%,\text{ave}}$ is the percent error, $\bar{\Delta}_{\dot{m}}$ is the mean difference between the time-averaged sensor mass flow and the set point (0.15 kg/s), and $\dot{m}_{\text{sp}}$ is the set point mass flow. Similarly the statistical precision of the set of 1-s measurements is given by the percent standard

Table 1 Best-case minimum velocity required for 1% mass flow accuracy as a function of the crossing angle

Crossing angle, 2θ	Minimum U for 1% mass flow accuracy, time averaged, m/s	Minimum U for 1% mass flow accuracy, 1-Hz measurement time, m/s
90 deg	21.5	60
60 deg	30	85
45 deg	40	110
37.7 deg	47	130
20 deg	88	245

deviation of the mass flow measurements, $\sigma_{\%}$. The overall sensor uncertainty $\varepsilon_{\%,1\,\mathrm{s}}$ is then estimated as the root-sum-square (independent) combination of the accuracy $\varepsilon_{\%,acc}$ and precision of $\sigma_{\%}$:

$$\varepsilon_{\%,1\,\mathrm{s}} = \sqrt{\varepsilon_{\%,\mathrm{ave}}^2 + \sigma_{\%}^2} \tag{14}$$

The predicted percentage uncertainty of the sensor measurements decreases with increasing velocity and the data in Fig. 10 extrapolate to mass flux sensor uncertainty at a 1 Hz readout rate to be <1% for velocities >60 m/s. The estimated sensor uncertainty depends on the crossing angle, and the minimum velocities for mass flow determination with <1% uncertainty in the time-averaged and 1-s measurement values are listed in Table 1 for a selection of crossing angles; note that 37.7 deg represents the crossing angle used in the aeroengine described in the companion paper [21]. Given the ideal environment of the wind tunnel, these are expected to be the best-case minimum velocities to achieve <1% accuracy for the mass flux measurements with this sensor design and data analysis scheme.

VIII. Conclusions

A fiber-coupled diode-laser mass flux sensor was designed, using oxygen as the absorbing species. The velocity is determined from the Doppler frequency shift between the absorption features of two split beams, and the density is measured from the magnitude of one of the absorption features. Scanned WMS-2f is used for the velocity measurement to reduce noise, while the density measurement relies upon the quantitative properties of direct absorption. A hybrid scanning operation is used to continuously alternate between direct and WMS scanning for each successive scan at an overall rate of 1 Hz.

The sensor's performance was assessed in a Stanford wind tunnel capable of generating velocities up to 23 m/s. Overall, the sensor obtained a time-averaged velocity which is within 0.25 m/s of the set point, and a 1-s standard deviation of 0.22 m/s. The sensor-measured time-averaged density is within 0.7% of the ambient density overall, and the 1-s standard deviation is 0.76%. The time-averaged mass flow measurement at the highest flow condition agrees within 1% of the set point value, and the 1-s percent standard deviation at the highest flow rate of 16.2 kg/s is 1.3%.

Acknowledgments

This research was supported by Pratt and Whitney. The authors would like to thank Stanford colleague Xin Zhou for his assistance during the early development of the sensor, and also Stanford Professor Peter Bradshaw for providing access to his wind tunnel to test the sensor's performance.

References

[1] Abernethy, R. B., Roberts, J., Adams, G., and Steurer, J., "In-Flight Thrust Determination," Society of Automotive Engineers, SAE AIR 1703, Report of the SAE Committee E-33, 1986.

[2] Williams, J. G., Steenken, W. G., and Yuhas, A. J., "Estimating Engine Airflow in Gas-Turbine Powered Aircraft with Clean and Distorted Inlet Flows," NASA CR-198052, 1996.

[3] Roberts, J. H., Beyerly, W. R., Mason, M. W., Glazier, J. R., and Wiley, R. H., "PW4084 Engine Testing in Altitude & Sea Level Test Facilities," *SAE Aerotechnology 1994*, SAE 94-2140, Los Angles, CA, Oct. 1994.

[4] Schmid, N. R., Leinhos, D. C., and Fottner, F., "Steady Performance Measurements of a Turbofan Engine with Inlet Distortions Containing Co- and Counterrotating Swirl from an Intake Diffuser for Hypersonic Flight," *Journal of Turbomachinery*, Vol. 123, No. 2, 2001, pp. 379–385.

[5] Allen, M. G., "Diode Laser Absorption Sensors for Gas-Dynamic and Combustion Flows," *Measurement Science and Technology*, Vol. 9, No. 4, 1998, pp. 545–562.

[6] Arroyo, M. P., and Hanson, R. K., "Absorption Measurements of Water Vapor Concentration, Temperature and Line-Shape Parameters Using a Tunable InGaAsP Diode Laser," *Applied Optics*, Vol. 32, No. 30, 1993, pp. 6104–6116.

[7] Philippe, L. C., and Hanson, R. K., "Laser Diode Wavelength-Modulation Spectroscopy for Simultaneous Measurement of Temperature, Pressure, and Velocity in Shock-Heated Oxygen Flows," *Applied Optics*, Vol. 32, No. 30, 1993, pp. 6090–6103.

[8] Miller, M. F., Kessler, W. J., and Allen, M. G., "Diode Laser-Based Air Mass Flux Sensor for Subsonic Aeropropulsion Inlets," *Applied Optics*, Vol. 35, No. 24, 1996, pp. 4905–4912.

[9] Furlong, E. R., Baer, D. S., and Hanson, R. K., "Combustion Control Using a Multiplex Diode-Laser Sensor System," *Proceedings of the Combustion Institute*, Vol. 26, 1996, pp. 2851–2858.

[10] Mihalcea, R. M., Baer, D. S., and Hanson, R. K., "Diode Laser Sensor for Measurements of CO, CO_2, and CH_4 in Combustion Flows," *Applied Optics*, Vol. 36, No. 33, 1997, pp. 8745–8752.

[11] Wang, J., Sanders, S. T., Jeffries, J. B., and Hanson, R. K., "Oxygen Measurements at High Pressures with Vertical Cavity Surface-Emitting Lasers," *Applied Physics B (Lasers and Optics)*, Vol. 72, No. 7, 2001, pp. 865–871.

[12] Webber, M. E., Claps, R., Englich, F. V., Tittel, F. K., Jeffries, J. B., and Hanson, R. K., "Measurements of NH_3 and CO_2 with Distributed-Feedback Diode Lasers Near 2.0 μm in Bioreactor Vent Gases," *Applied Optics*, Vol. 40, No. 24, 2001, pp. 4395–4403.

[13] Furlong, E. R., Mihalcea, R. M., Webber, M. E., Baer, D. S., Hanson, R. K., and Parr, T. P., "Diode Laser Sensor System for Closed-Loop Control of a 50-kw Incinerator," *Proceedings of SPIE: The International Society for Optical Engineering*, Vol. 3172, 1997, pp. 324–330.

[14] Upschulte, B. L., Miller, M. F., and Allen, M. G., "Diode Laser Sensor for Gasdynamic Measurements in a Model Scramjet Combustor," *AIAA Journal*, Vol. 38, No. 7, 2000, pp. 1246–1252.

[15] Mattison, D. W., Brophy, C. M., Sanders, S. T., Ma, L., Hinckley, K. M., Jeffries, J. B., and Hanson, R. K., "Pulse Detonation Engine Characterization and Control Using Tunable Diode Laser Sensors," *Journal of Propulsion and Power*, Vol. 19, No. 4, 2003, pp. 568–572.

[16] Mattison, D. W., Jeffries, J. B., Hanson, R. K., Steeper, R. R., DeZilwa, S., Dec, J. E., Sjoberg, M., and Hwang, W., "In-Cylinder Gas Temperature and Water Concentration Measurements in HCCI Engines Using a Multiplexed-Wavelength Diode-Laser System: Sensor Development and Initial Demonstration," *Proceedings of the Combustion Institute*, Vol. 31, 2007, pp. 791–798.

[17] Wehe, S. D., Baer, D. S., Hanson, R. K., and Chadwick, K. M., "Measurements of Gas Temperature and Velocity in Hypervelocity Flow Using Diode-Laser Sensors," AIAA Paper 98-2699, June 1998.

[18] Mohamed, A., Rosier, B., Henry, D., Louvet, Y., and Varghese, P. L., "Tunable Diode Laser Measurements on Nitric Oxide in a Hypersonic Wind Tunnel," *AIAA Journal*, Vol. 34, No. 3, 1996, pp. 494–499.

[19] Mohamed, A., Rosier, B., Sagnier, P., Louvet, Y., and Bize, D., "Application of Infrared Diode Laser Absorption Spectroscopy to the F4 High Enthalpy Wind Tunnel," *Aerospace Science and Technology*, Vol. 2, No. 4, 1998, pp. 241–250.

[20] Hanson, R. K., "Spectroscopy-Based Thrust Sensor for High-Speed Gaseous Flows," U.S. Patent No. 5178002, filed Oct. 1991, granted Jan. 1993.

[21] Lyle, K. H., Jeffries, J. B., and Hanson, R. K., "Diode-Laser Sensor for Air-Mass Flux 2: Nonuniform Flow Modeling and Aeroengine Tests," *AIAA Journal*, Vol. 45, No. 9, 2007, pp. 2213–2223.

[22] Ritter, K. J., and Wilkerson, T. D., "High-Resolution Spectroscopy of the Oxygen A Band," *Journal of Molecular Spectroscopy*, Vol. 121, No. 1, 1987, pp. 1–19.

[23] Brown, L. R., and Plymate, C., "Experimental Line Parameters of the Oxygen A Band at 760 nm," *Journal of Molecular Spectroscopy*, Vol. 199, No. 2, 2000, pp. 166–179.

[24] Rothman, L. S., Barbe, A., Benner, D. C., Brown, L. R., Camy-Peyret, C., Carleer, M. R., Chance, K., Clerbaux, C., Dana, V., Devi, V. M., Fayt, A., Flaud, J.-M., Gamache, R. R., Goldman, A., Jacquemart, D., Jucks, K. W., Lafferty, W. J., Mandin, J.-Y., Massie, S. T., Nemtchinov, V., Newnham, D. A., Perrin, A., Rinsland, C. P., Schroeder, J., Smith, K. M., Smith, M. A. H., Tang, K., Toth, R. A., Auwera, J. V., Varanasi, P., and Yoshino, K., "The HITRAN Molecular Spectroscopic Database: Edition of 2000 Including Updates Through 2001," *Journal of Quantitative Spectroscopy and Radiative Transfer*, Vol. 82, Nos. 1–4, 2003, pp. 5–44.

[25] Reid, J., and Labrie, D., "Second-Harmonic Detection with Tunable Diode Lasers—Comparison of Experiment and Theory," *Applied*

Physics B, Photophysics and Laser Chemistry, Vol. 26, No. 3, 1981, pp. 203–210.

[26] Dharamsi, A. N., and Bullock, A. M., "Applications of Wavelength-Modulation Spectroscopy in Resolution of Pressure and Modulation Broadened Spectra," *Applied Physics B (Lasers and Optics)*, Vol. 63, No. 3, 1996, pp. 283–292.

[27] Kluczynski, P., and Axner, O., "Theoretical Description Based on Fourier Analysis of Wavelength-Modulation Spectrometry in Terms of Analytic and Background Signals," *Applied Optics*, Vol. 38, No. 27, 1999, pp. 5803–5815.

[28] Liu, J. T. C., Jeffries, J. B., and Hanson, R. K., "Wavelength Modulation Absorption Spectroscopy with 2f Detection Using Multiplexed Diode Lasers for Rapid Temperature Measurements in Gaseous Flows," *Applied Physics B (Lasers and Optics)*, Vol. 78, Nos. 3–4, 2004, pp. 503–511.

[29] Silver, J. A., "Frequency-Modulation Spectroscopy for Trace Species Detection: Theory and Comparison Among Experimental Methods," *Applied Optics*, Vol. 31, No. 6, 1992, pp. 707–717.

[30] Weldon, V., O'Gorman, J., Pérez-Camacho, J. J., McDonald, D., Hegarty, J., Connolly, J. C., Morris, N. A., Martinelli, R. U., and Abeles, J. H., "Laser Diode Based Oxygen Sensing: A Comparison of VCSEL and DFB Laser Diodes Emitting in the 762 nm Region," *Infrared Physics and Technology*, Vol. 38, No. 6, 1997, pp. 325–329.

N. Clemens
Associate Editor